Supporting Information

Near-Infrared-II Photothermal Conversion and Magnetic Dynamic Regulation in [Ln₃Rad₂] Aggregation by Rigidity Modification of Nitronyl Nitroxide

Hongdao Li*[ab], Chaoyi Jin[b], Jing Han[b], Jianke Tang[a], Xiaofeng Han*[c], Zhenjun Song*[d,b]

[a] *Department of Chemistry and Chemical Engineering, Taiyuan Institute of Technology, Taiyuan 030008, China*

[b] *Department of Chemistry, Key Laboratory of Advanced Energy Materials Chemistry and Tianjin Key Laboratory of Metal and Molecule-based Material Chemistry, College of Chemistry, Nankai University, Tianjin 300071, China*

[c] *Department of Chemistry and Materials Science, Inner Mongolia Minzu University, Tongliao 028000, China*

[d] *School of Pharmaceutical and Materials Engineering, Taizhou University, Taizhou 318000, China*

Table of Contents

Experimental Procedures

Materials and Physical measurements.

All the reagents and solvents were commercially available and used as received. FT-IR data were recorded on a Vector27 Bruker Spectrophotometer with KBr pellets in the 4000-400 cm^{-1} region. Elemental analyses for C, H, and N were recorded on a Perkin-Elmer 240C analyzer. The PXRD data were collected on a Bruker Advance D8 diffractometer with Cu radiation (λ = 1.54056 Å) at room temperature. TGA data were obtained on a STA 449C thermal analysis system under N_2 atmosphere. Electron paramagnetic resonance (EPR) data were collected in the X-band at room temperature on a Bruker A300 spectrometer. X-Ray photoelectron spectroscopy (XPS) measurements were performed on a Thermo Fisher Scientific ESCALAB Xi+ system with an Al Kα source. Magnetic data were probed utilizing a Quantum Design SQUID VSM device and were corrected for the diamagnetism with Pascal's constants and all samples holder.

Photothermal conversion: 275 mg of **1-Dy/2-Dy** thin round layer (thickness of 1.5 mm) with the largest possible surface area (diameter of 1.5 cm) placed on a tripod at a distance of 20 cm from the 1064 or 915 nm laser (0.1 W cm^{-2}). The infrared camera was used to capture the infrared videos of the **1-Dy/2-Dy** sample when the illumination was on/off. The infrared photos and real-time temperatures were extracted from the video.

Synthesis of NIT4bpym and NITPzCH$_2$IM.

NIT4bpym and NITPzCH$_2$IM were synthesized according to the previous method. [S1]

Synthesis of [Gd$_3$(hfac)$_9$(NIT4bpym)$_2$]$_2$·4CH$_2$Cl$_2$·C$_6$H$_{14}$ (1-Gd), [Dy$_3$(hfac)$_9$(NIT4bpym)$_2$] (1-Dy) and [Dy$_3$(hfac)$_9$(NITPzCH$_2$IM)$_2$]·2CH$_2$Cl$_2$ (2-Dy)

Ln(hfac)$_3$·2H$_2$O (0.015 mmol) was suspended in 25 mL of n-hexane to reflux for 4 hours until most of them dissolved, and a solution of NIT4bpym or NITPzCH$_2$IM (0.01 mmol) in 5 mL of CH$_2$Cl$_2$ was introduced with stirring. After 30 min, the resulting blue solution was filtered, and the above filtrate could volatilize slowly at ambient temperature to generate azury crystals.

1-Gd: Yield 81%. C$_{158}$H$_{94}$F$_{108}$Gd$_6$N$_{16}$O$_{44}$ (5915.99 g/mol) (without solvent molecules): calcd. C 32.07, H 1.60, N 3.78; found. C 32.10, H 1.62, N 3.76; FT-IR (KBr): 3408(s), 1618(m), 1601 (m), 1326 (m), 1135 (s), 1043 (s), 960 (s), 858 (s), 763 (m), 548 (s), 521(s) cm^{-1}.

1-Dy: Yield 85%. $C_{79}H_{47}Dy_3F_{54}N_8O_{22}$ (2973.74 g/mol): calcd. C 31.90, H 1.59, N 3.76; found. C 31.88, H 1.60, N 3.74; FT-IR (KBr): 3409(s), 1618(m), 1602 (m), 1326 (m), 1135 (s), 1043 (s), 960 (s), 859 (s), 763 (m), 547 (s), 520(s) cm^{-1}.

2-Dy: Yield 82%. $C_{75}H_{51}Dy_3F_{54}N_{12}O_{22}$ (2985.77 g/mol) (without solvent molecules): calcd. C 30.17, H 1.72, N 5.62; found. C 30.19, H 1.71, N 5.63; FT-IR (KBr): 3398(s), 1595(m), 1621 (m), 1310 (m), 1056 (s), 1003 (s), 987 (s), 845 (s), 785 (m), 531 (s), 495(s) cm^{-1}.

X-ray Crystallography

Single-crystal structure investigations were performed on a Rigaku Saturn diffractometer equipped with a CCD area detector and graphite-monochromated Mo/Kα radiation ($\lambda = 0.71073$ Å) at 193 K or 223 K. Empirical absorption corrections based on symmetry equivalent reflections were applied. The structure solution was done with direct methods using SHELXS-2014 [S2], and structure refinements were performed by a full-matrix least-squares procedure using SHELXL-2014 [S3]. Anisotropic thermal parameters were assigned to all non-hydrogen atoms. Hydrogen atoms were placed in calculated, ideal positions and were refined isotropically as riding on their respective C atoms. In **1-Gd** and **2-Dy**, free solvent molecules (C_6H_{14} and CH_2Cl_2) were highly disordered and were unable to be located and refined. The diffuse electron densities resulting from these residual molecules were removed from the data set using the SQUEEZE routine of PLATON and refined further using the data generated. The final formulas of **1-Gd** and **2-Dy** were calculated from the SQUEEZE results [S4] and combined with number of electrons. CCDC 2347435 (**1-Gd**), 2347436 (**1-Dy**) and 2371970 (**2-Dy**) contain the supplementary crystallographic data for this paper. These data can be obtained free of charge from The Cambridge Crystallographic Data Centre.

Table S1. The crystal data and refinement details of **1-Gd**, **1-Dy** and **2-Dy**.

Complex	1-Gd	1-Dy	2-Dy
Empirical formula	$C_{158}H_{94}F_{108}Gd_6N_{16}O_{44}$	$C_{79}H_{47}Dy_3F_{54}N_8O_{22}$	$C_{75}H_{51}Dy_3F_{54}N_{12}O_{22}$

Mr	5915.99	2973.74	2985.77
T (K)	193.15	193.15	223
Crystal system	triclinic	triclinic	monoclinic
Space group	$P\bar{1}$	$P\bar{1}$	$P2_1/n$
a /Å	21.319(4)	11.3435(16)	21.6876(11)
b /Å	24.086(4)	17.940(3)	20.3917(12)
c /Å	25.171(5)	27.416(3)	28.1940(17)
α /°	75.925(7)	95.376(5)	90
β /°	78.350(7)	101.823(4)	98.918(2)
γ /°	74.502(7)	96.555(5)	90
V /Å^3	11951(4)	5385.7(13)	12318.0(12)
Z	2	2	4
D_{calcd} /g cm^{-3}	1.644	1.834	1.610
θ /°	3.954-49.998	3.704-55.032	4.228-50.052
$F(000)$	5724	2874	5780.0
Reflections collected	210286	114171	119355
Unique reflns/R_{int}	41602/0.0891	24793/0.0711	21193/0.1393
GOF (F^2)	1.043	1.029	1.022
R_1, wR_2 ($I > 2\sigma(I)$)	0.0575, 0.1434	0.0703, 0.2001	0.0711, 0.1395
R_1, wR_2 (all data)	0.0811, 0.1601	0.0923, 0.2288	0.1166, 0.1651

Table S2. The important bond lengths [Å] and angles [°] for **1-Gd**, **1-Dy** and **2-Dy**.

Complex	**1-Gd**	**1-Dy**	**2-Dy**
Ln–O(rad)	2.395(4)-2.369(4)	2.336(5), 2.341(5)	2.341(6), 2.290(7)

Ln–O(hfac)	2.337(5)–2.414(5)	2.295(7)-2.363(5)	2.299(7)-2.367(7)
Ln–N	2.535(6)-2.563(6)	2.505(7)-2.554(6)	2.472(8)-2.567(8)
O(rad)–Ln–O(rad)	139.24(16), 140.60(17)	136.37(19)	140.3(3)
N–Ln–N	62.8(2)-63.5(2)	63.70(18), 64.2(2)	72.1(3), 73.1(3)

Table S3 SHAPE analysis for complex **1-Gd**.

	SAPR-8	TDD-8	BTPR-8
Gd1	2.378	**0.216**	2.562
Gd2	2.709	**0.253**	2.303
Gd3	**0.405**	2.400	2.386
Gd4	**0.726**	1.384	1.985
Gd5	**1.071**	1.395	1.908
Gd6	1.486	1.578	**1.261**

Table S4 SHAPE analysis for complex **1-Dy**.

	SAPR-8	TDD-8	BTPR-8
Dy1	**0.505**	2.025	2.035
Dy2	1.305	**0.656**	1.952
Dy3	**0.512**	2.109	2.408

Table S5 SHAPE analysis for complex **2-Dy**.

SAPR-8	TDD-8	BTPR-8	JBTPR-8

Dy1	**0.340**	2.272	1.928	2.492
Dy2	3.441	**0.780**	1.857	2.259
Dy3	**0.396**	1.732	1.951	2.227

SAPR-8 (D_{4d}): Square antiprism;   TDD-8 (D_{2d}): Triangular dodecahedron;

BTPR-8 (C_{2v}): Biaugmented trigonal prism; JBTPR-8 (C_{2v}): Biaugmented trigonal prism J50
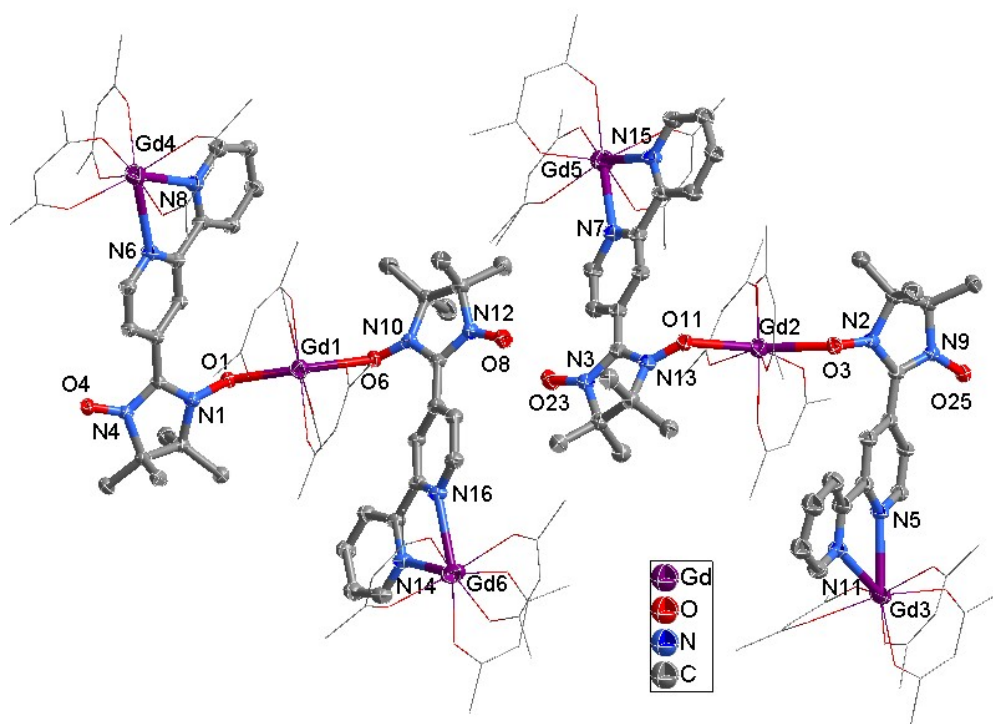
Figure S1. Molecular structure of the trinuclear **1-Gd**. The H and F atoms and solvent molecules are elided for clearness. Ellipsoids are set at the 50% probability levels.
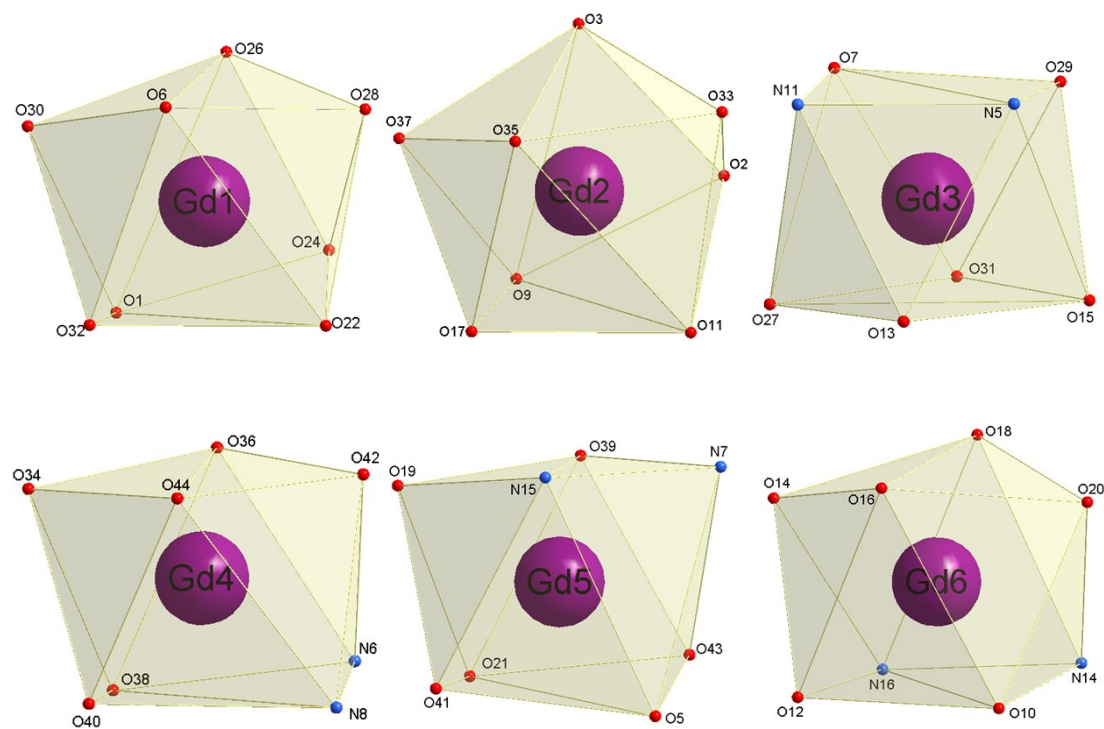
Figure S2. Coordination environment of six Gd[III] ions in compound **1-Gd**.
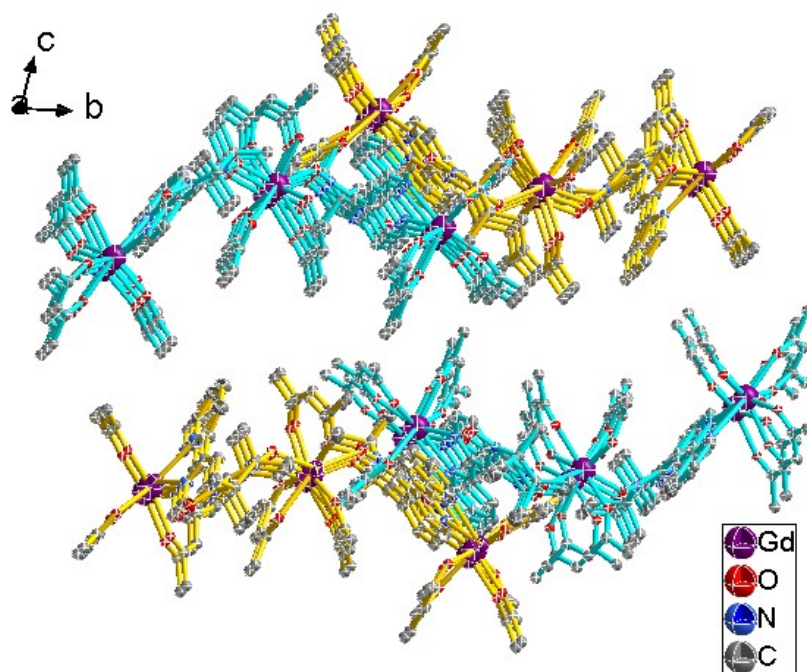
Figure S3. 3D packing pattern along the *a*-axis direction of **1-Gd**. The H and F atoms and solvent molecules are elided for clearness. Ellipsoids are set at the 50% probability levels.
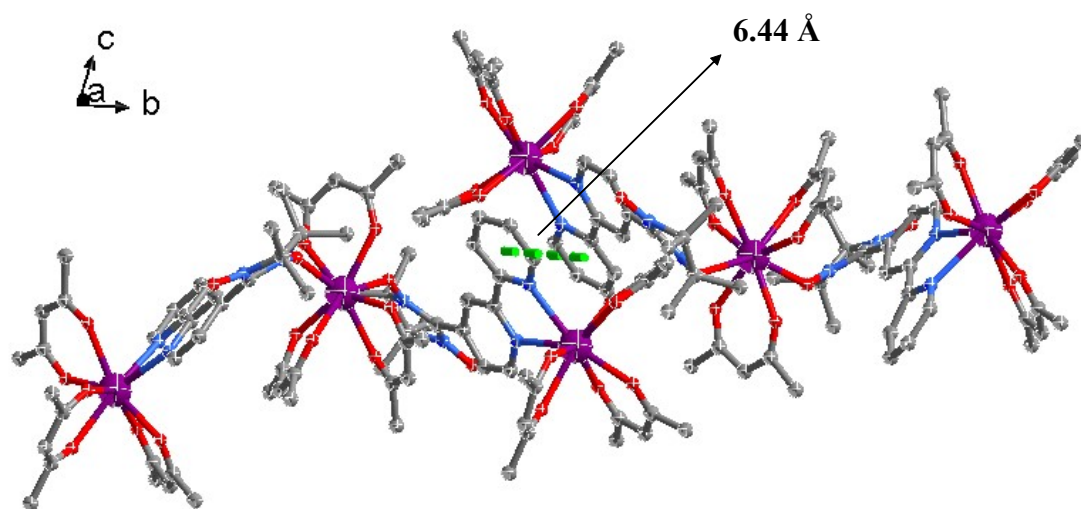
Figure S4. Adjacent pyridine ring centers with distance of 6.44 Å of **1-Gd**.
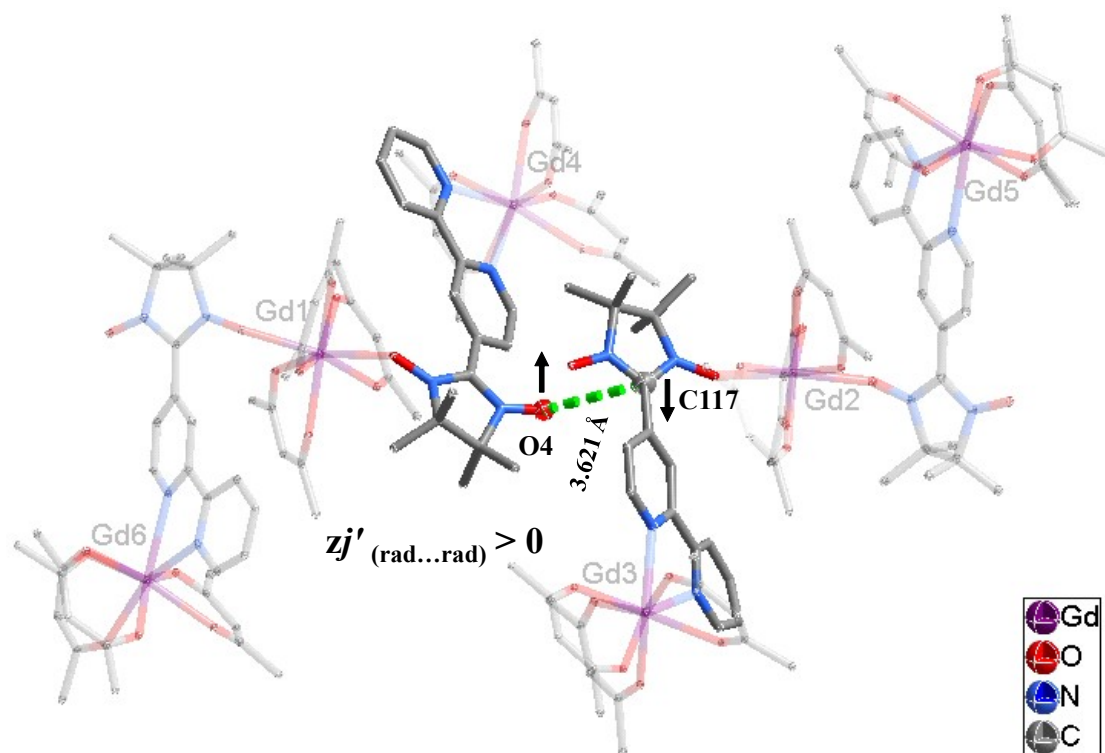
Figure S5. Packing pattern of **1-Gd** with the alternating spin densities in O4 (nitroxyl)-C117 (sp^2) leading to ferromagnetic interaction (zj').
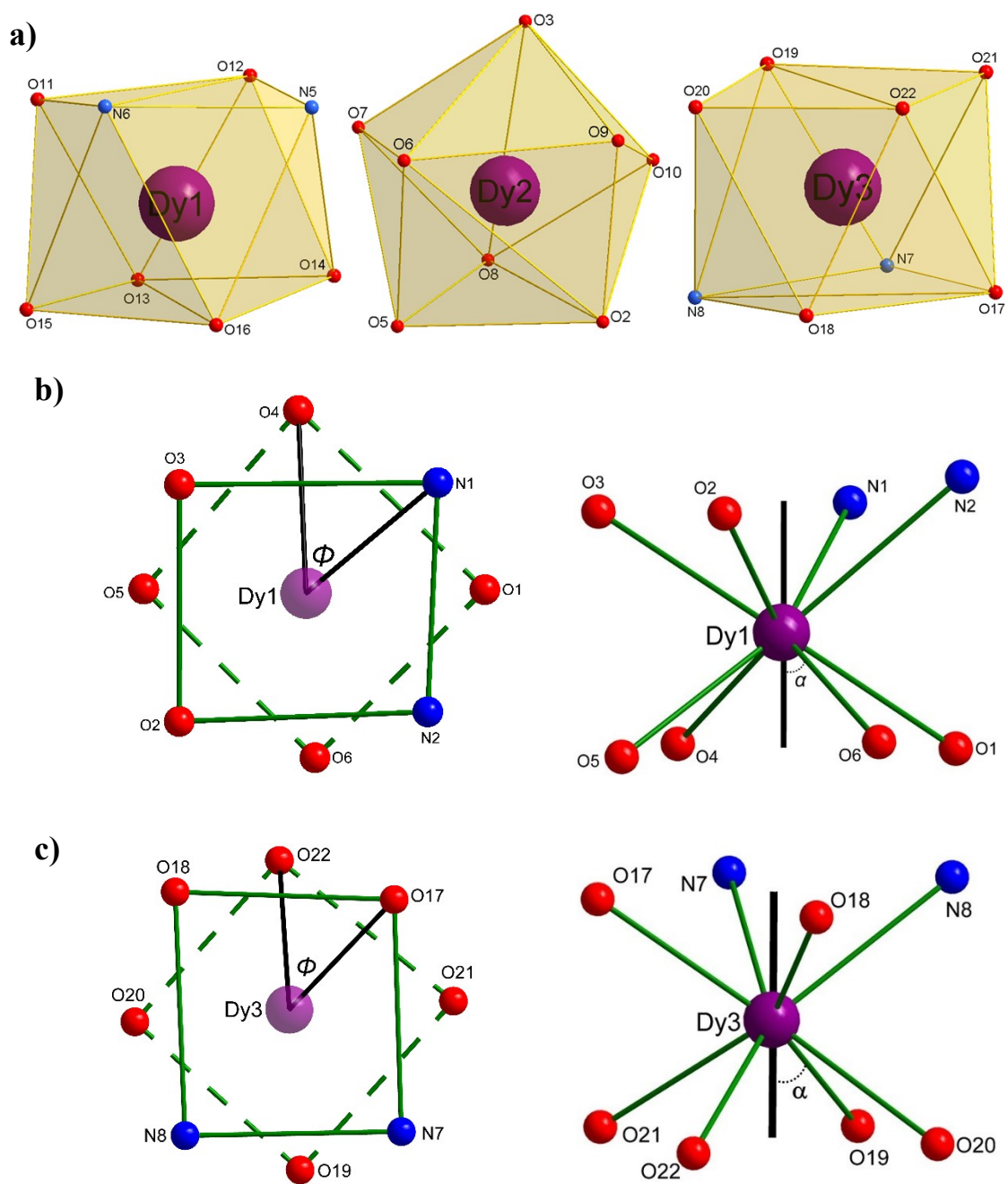
Figure S6. (a) Coordination environment of three Dy^{III} ions in compound **1-Dy**. (b)(c)   square-antiprismatic environment with angle Φ between the diagonals of the two squares. Angle α between the $S8$ axis and a Dy–O/N vector.
(Dy1: $\Phi = 45.12°$ and $\alpha = 55.73°$; Dy3: $\Phi = 44.96°$ and $\alpha = 56.14°$)
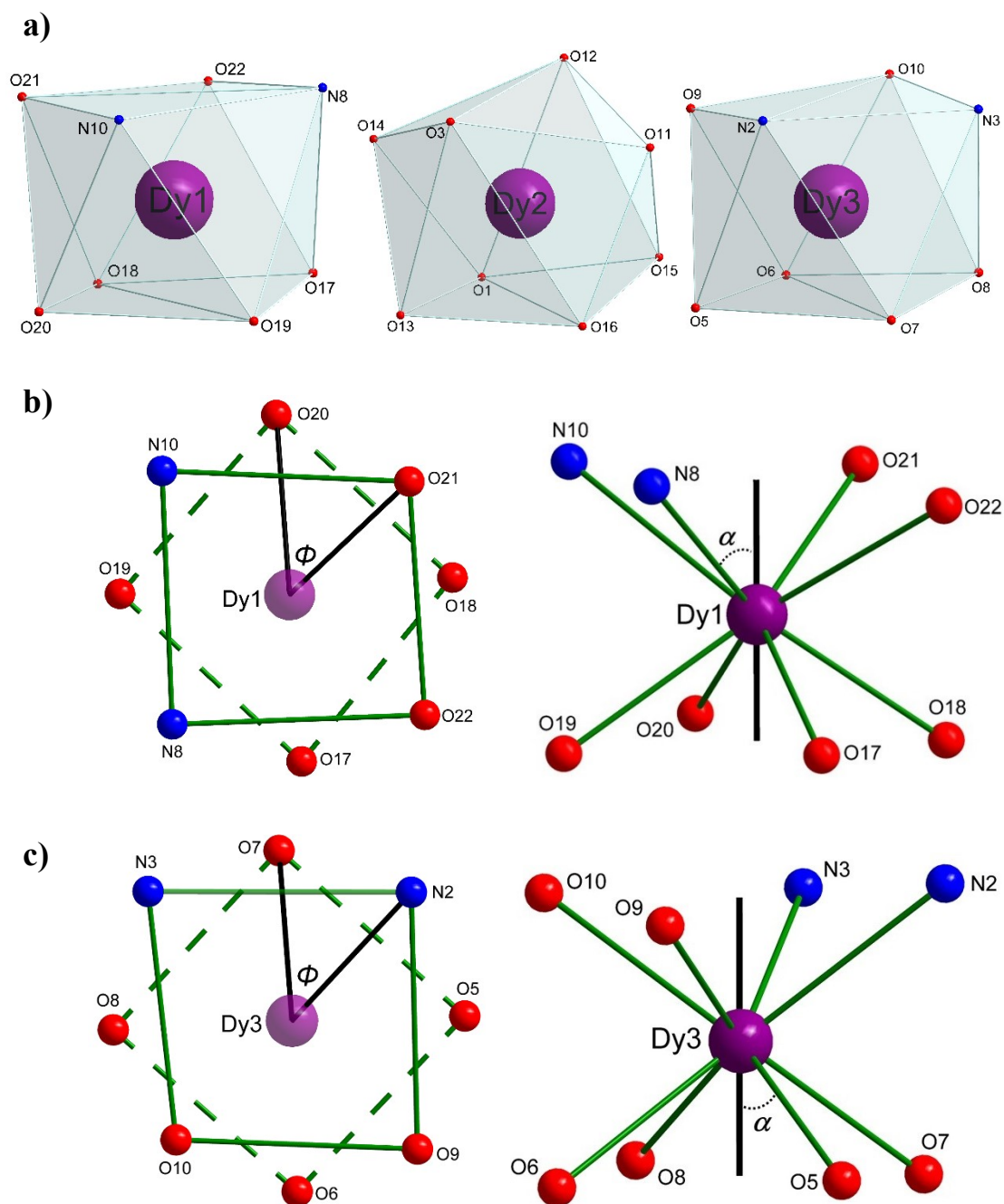
Figure S7. (a) Coordination environment of three Dy^{III} ions in compound **2-Dy**. (b)(c) square-antiprismatic environment with angle Φ between the diagonals of the two squares. Angle α between the $S8$ axis and a Dy–O/N vector.

(Dy1: $\Phi = 45.01°$ and $\alpha = 57.03°$; Dy3: $\Phi = 45.04°$ and $\alpha = 56.85°$)
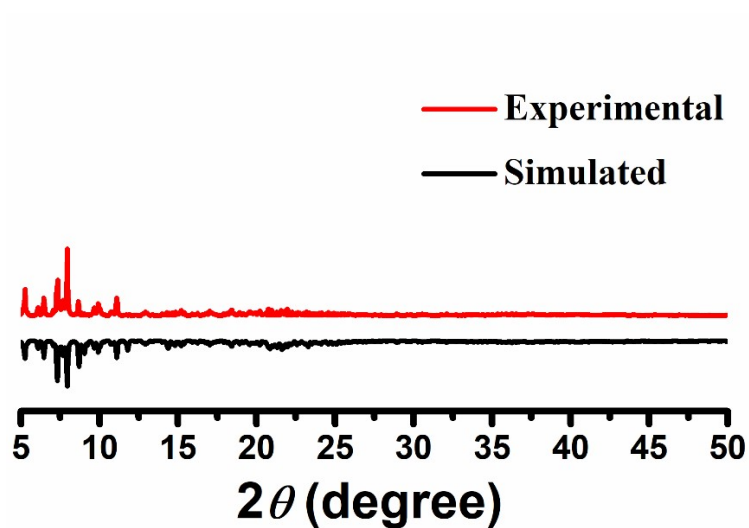
Figure S8. Powder X-ray diffraction pattern of **1-Gd** at 298 K, together with the calculated pattern from the crystal structure data.
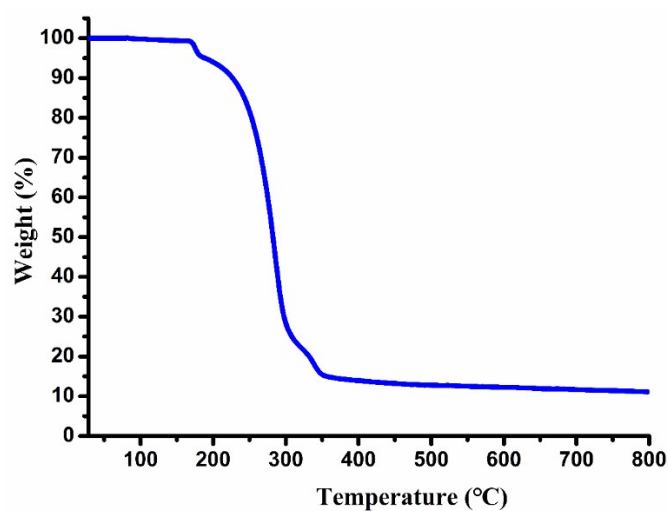
Figure S9. Thermogravimetric curves of **1-Dy** in N_2 atmosphere.

Thermogravimetric analysis was conducted from room temperature to 800 °C under N_2 atmosphere. A plateau up to ca. 168 °C, implying that was stable up to 168 °C. After the plateau, **1-Dy** began to decompose.
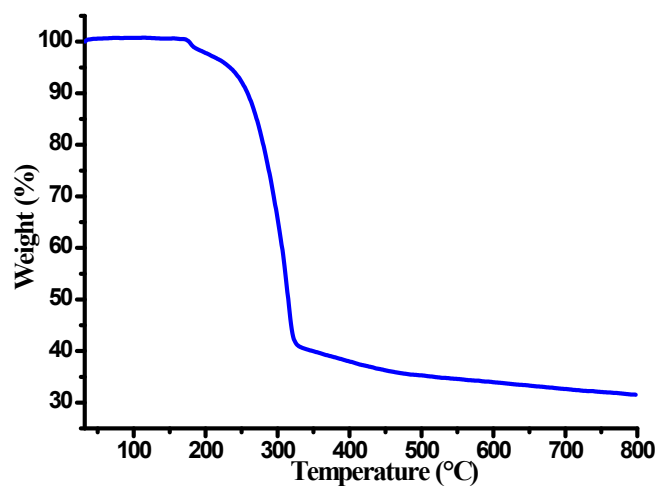
Figure S10. Thermogravimetric curves of **2-Dy** in N_2 atmosphere.

Thermogravimetric analysis was conducted from room temperature to 800 °C under N_2 atmosphere. A plateau up to ca. 173 °C, then, **2-Dy** began to decompose. Since the dichloromethane solvent is extremely volatile and has been volatilized before the thermogravimetric test, no weight loss was detected.
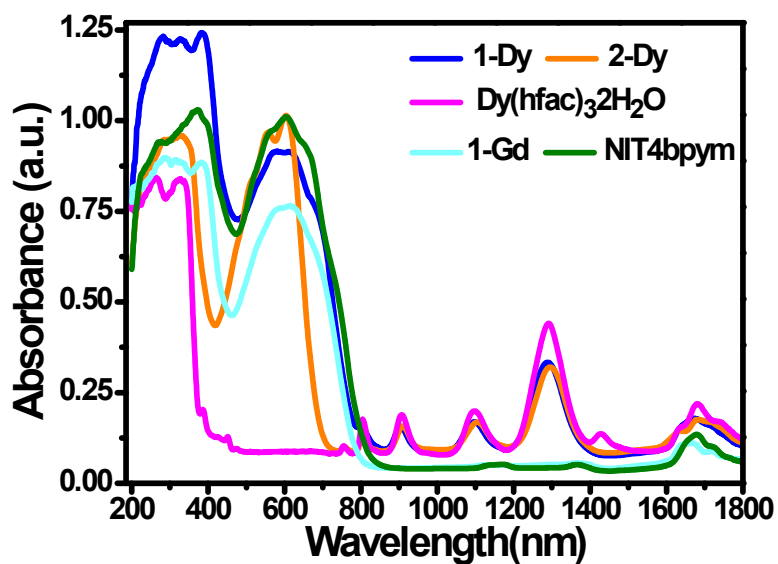
Figure S11. UV-Vis-NIR absorption of **1-Dy**, **2-Dy**, **1-Gd**, Dy(hfac)$_3$·2H$_2$O and NIT4bpym powder samples.
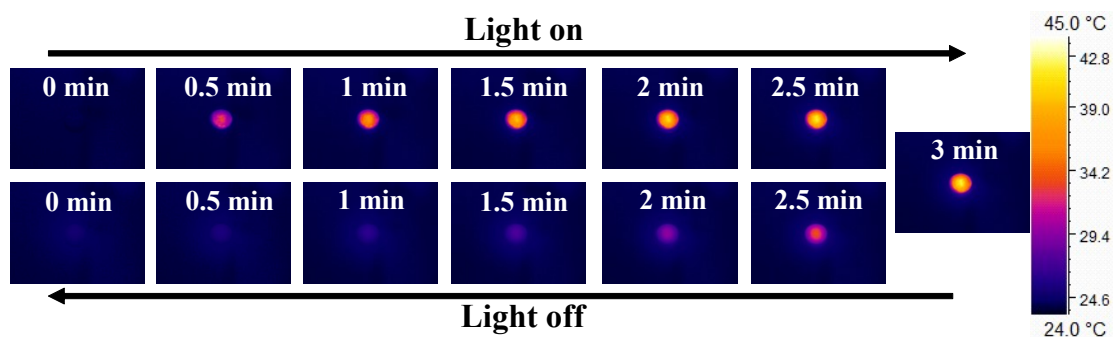
Figure S12. IR thermal images of **1-Dy** powder sample (275 mg) under 915 nm (0.1 W cm^{-2}) laser irradiation and then turned off.
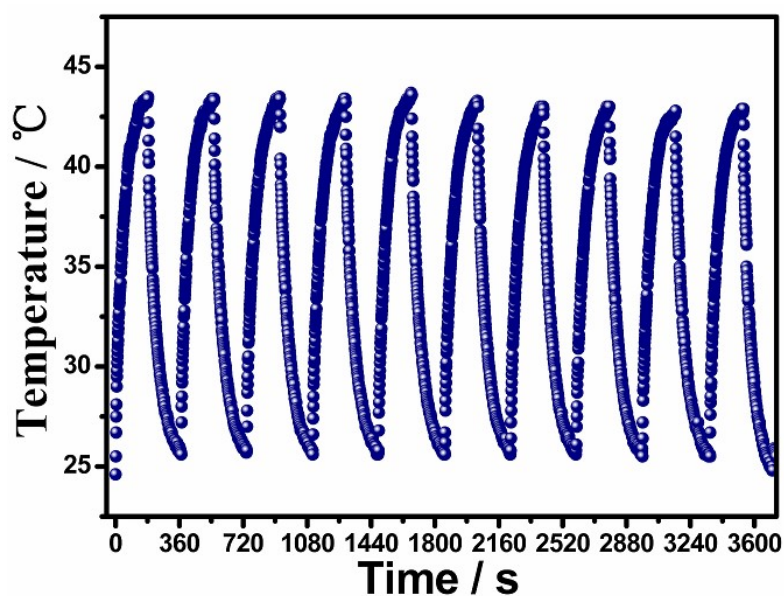
Figure S13. Anti-photobleaching performance of **1-Dy** powder sample during ten circulations of heating-cooling under 915 nm (0.1 W cm^{-2}) laser irradiation.
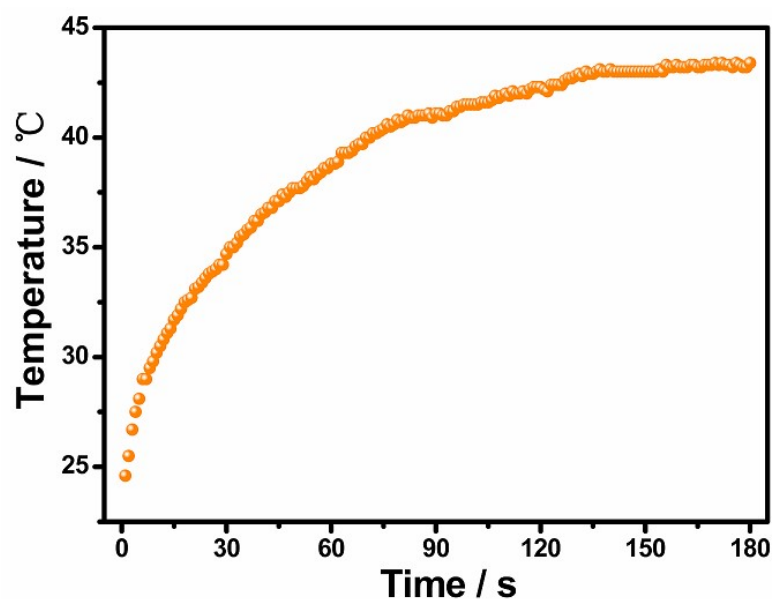
Figure S14. Photothermal conversion behavior of **1-Dy** powder under 915 nm (0.1 W cm^{-2}) laser irradiation within 3 minutes.
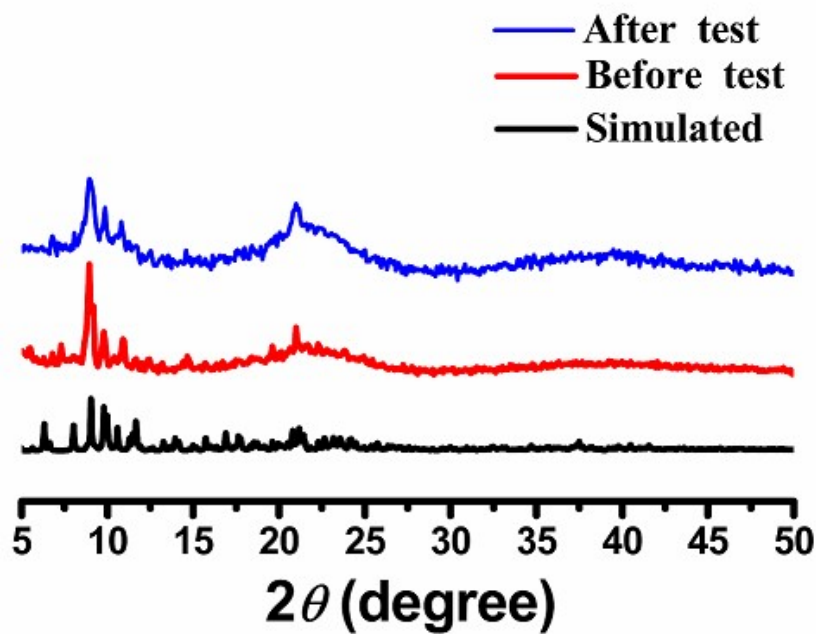
Figure S15. PXRD patterns of **1-Dy** theoretical parameter, before and after the photothermal test.
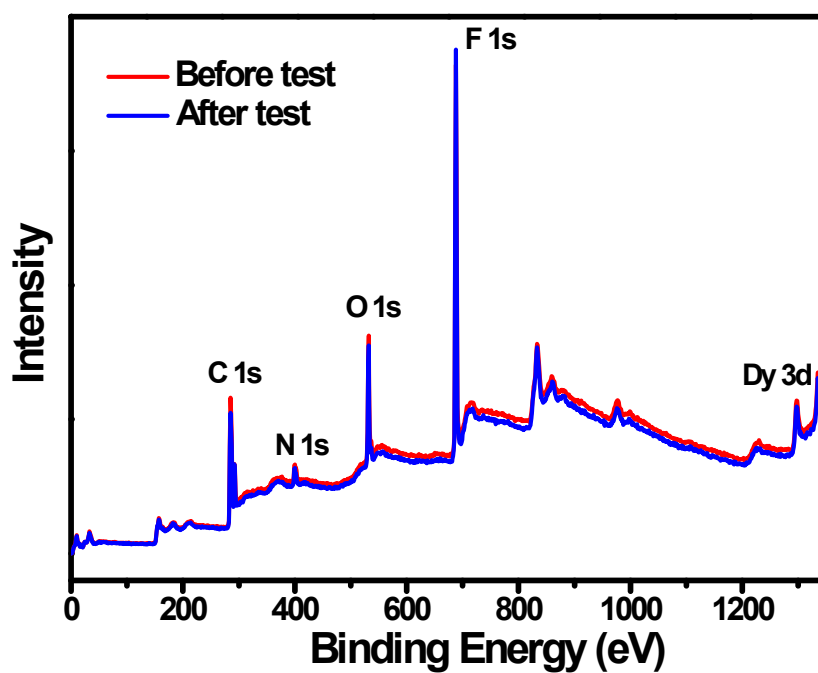
Figure S16. XPS spectra of **1-Dy** before and after the photothermal test.
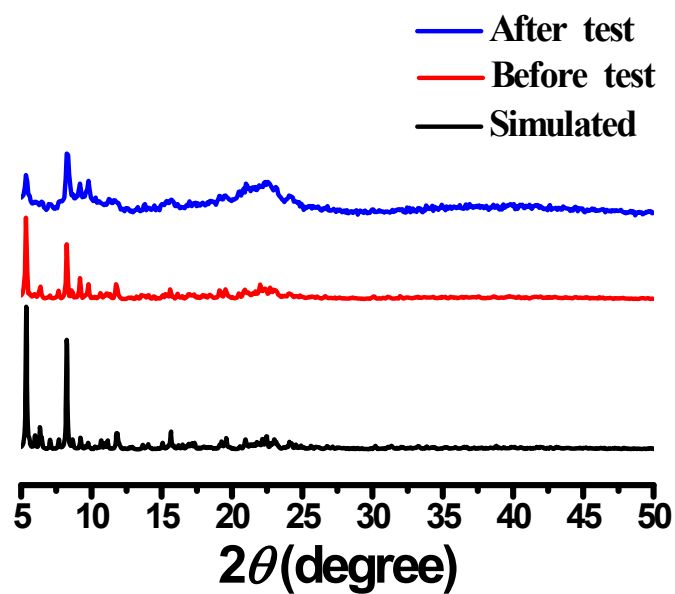
Figure S17. PXRD patterns of **2-Dy** theoretical parameter, before and after the photothermal test.
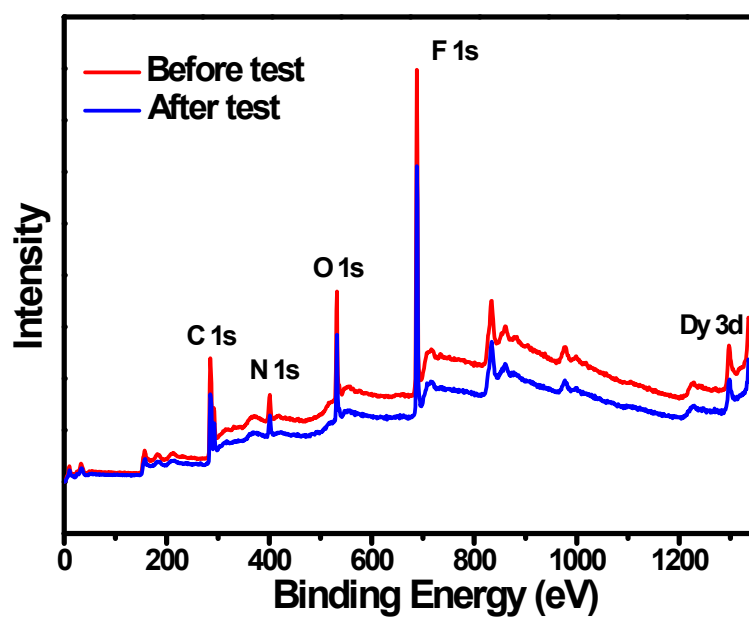
Figure S18. XPS spectra of **2-Dy** before and after the photothermal test.
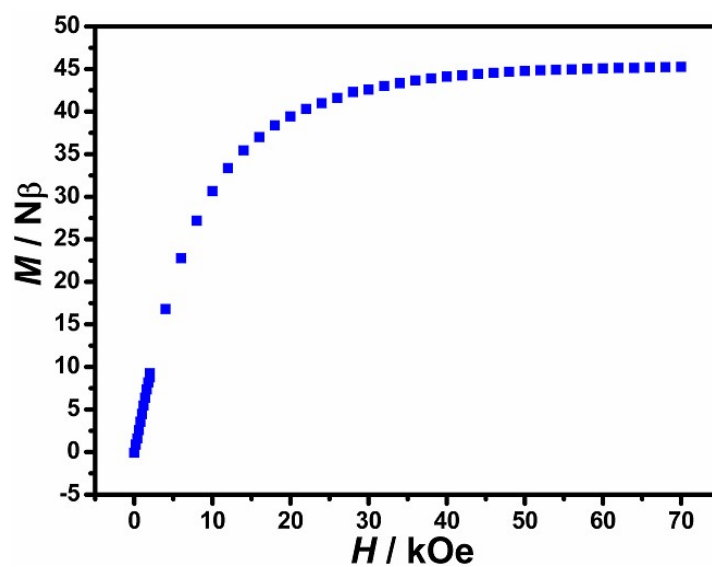
Figure S19. Field dependence of the magnetization for **1-Gd** at 2 K.
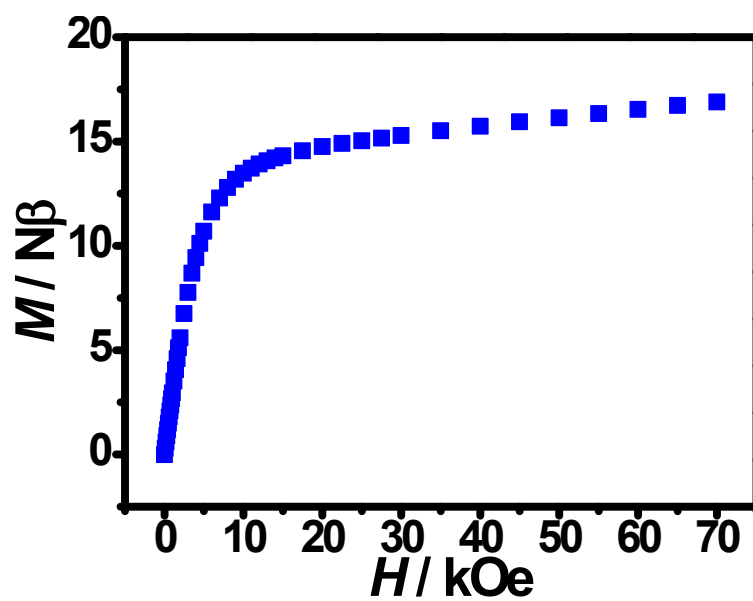
Figure S20. Field dependence of the magnetization for **1-Dy** at 2 K.
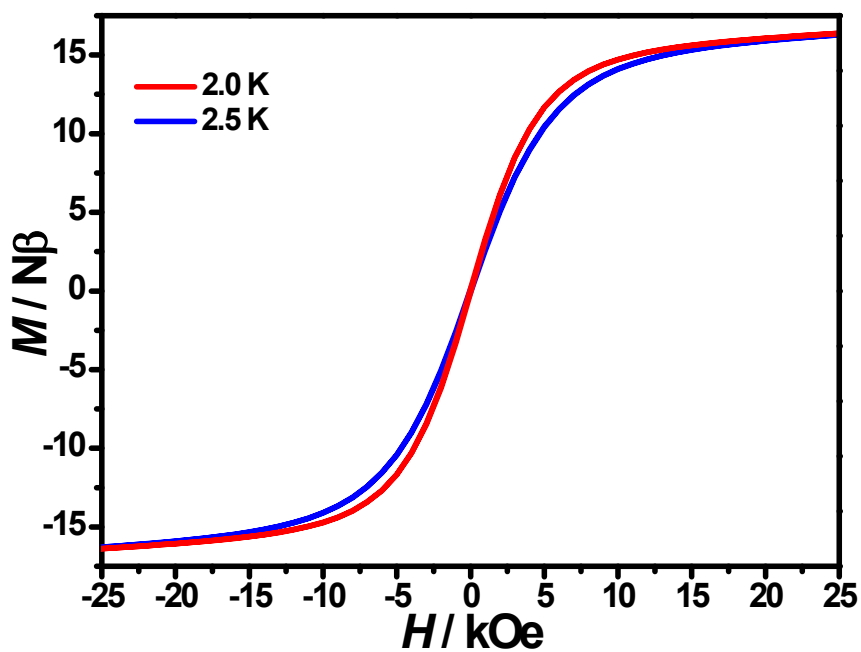
Figure S21. Field dependence of magnetization for **1-Dy** at a field sweep rate of 700 Oe/s.
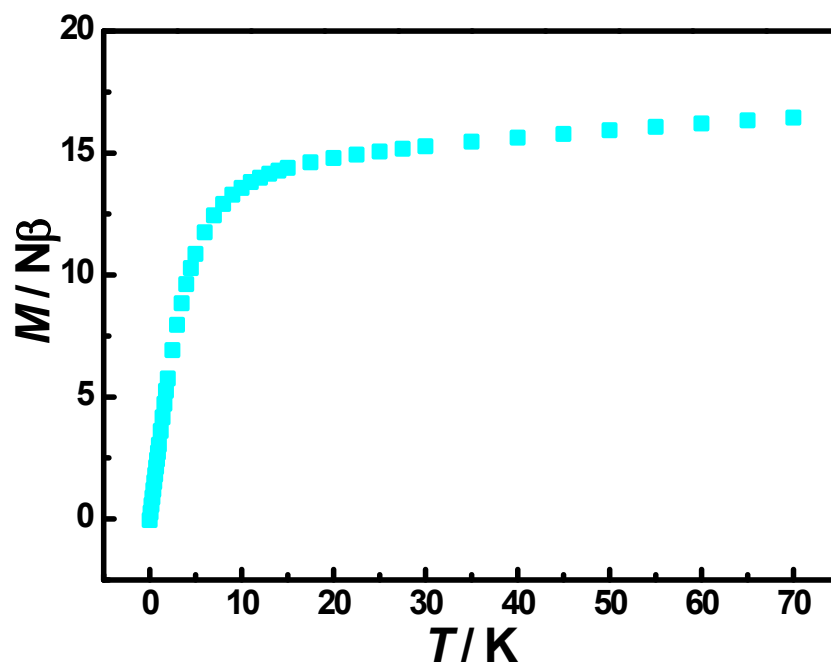
Figure S22. Field dependence of the magnetization for **2-Dy** at 2 K.
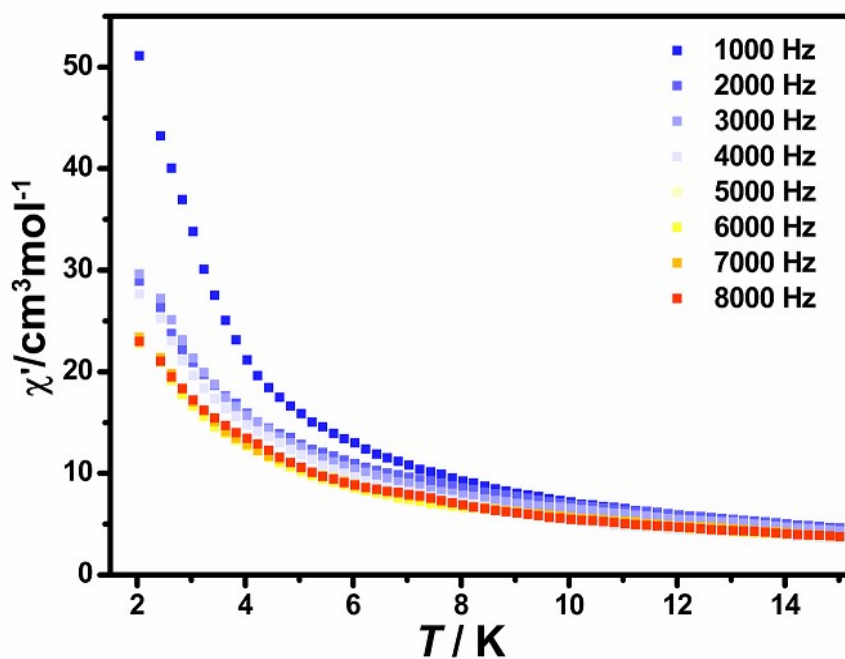
Figure S23. χ' (T) plot of **1-Dy** for frequence between 1000 and 8000 Hz in 0 Oe dc field.
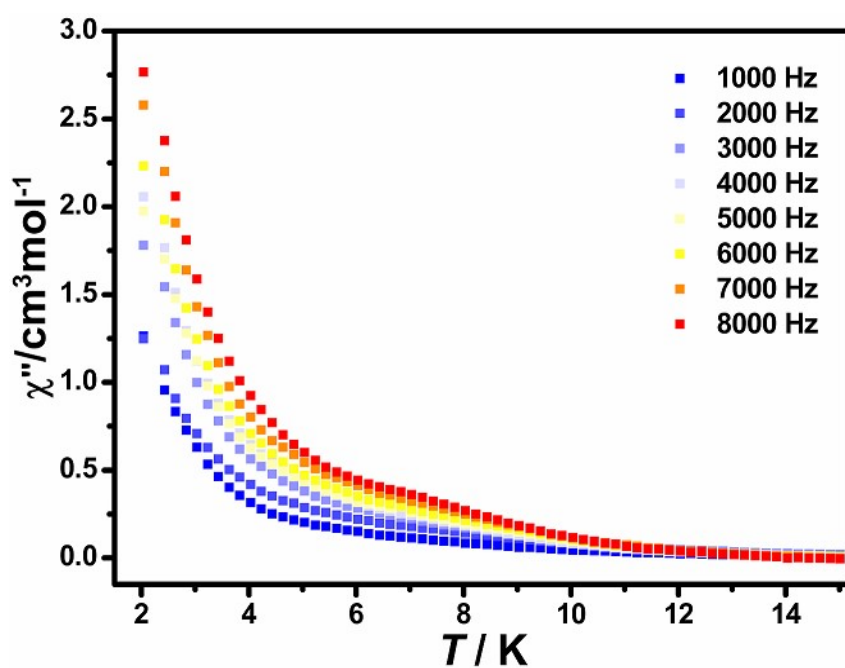
Figure S24. χ'' (T) plot of **1-Dy** for frequence between 1000 and 8000 Hz in 0 Oe dc field.
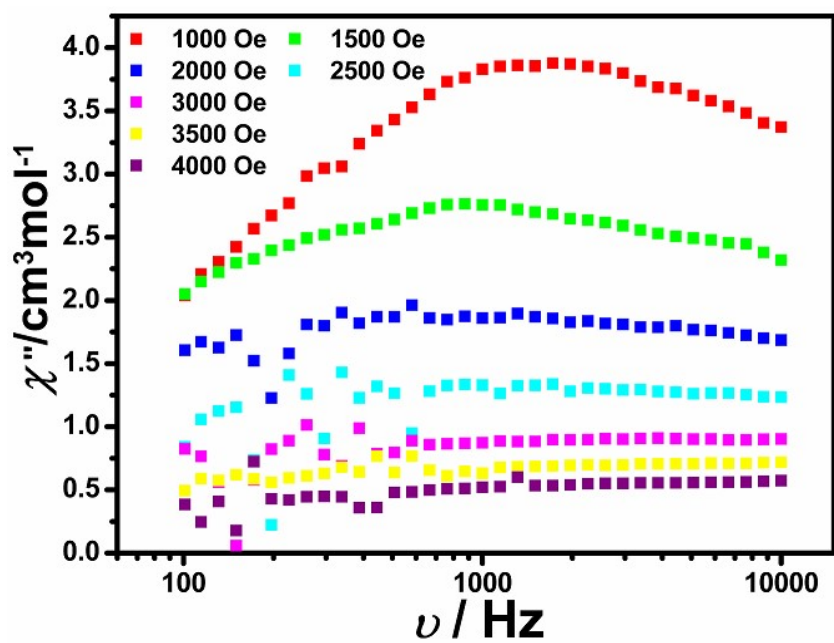
Figure S25. Frequency-dependent ac magnetic susceptibilities under externally applied dc fields at 2K for **1-Dy**.
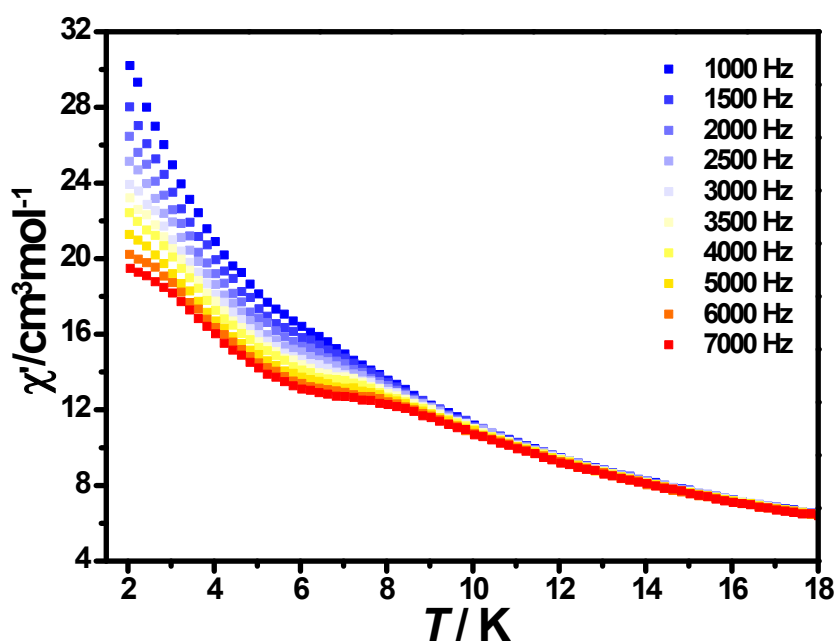
Figure S26. χ' (T) plot of **1-Dy** for frequence between 1000 and 7000 Hz in 1000 Oe dc field.
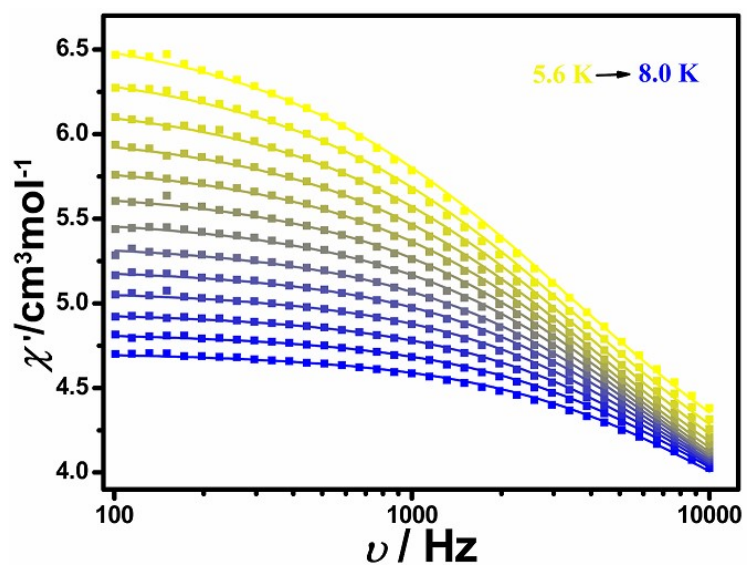
Figure S27. χ' (v) plot of **1-Dy** for temperature between 5.6 and 8.0 K in 1000 Oe dc field.
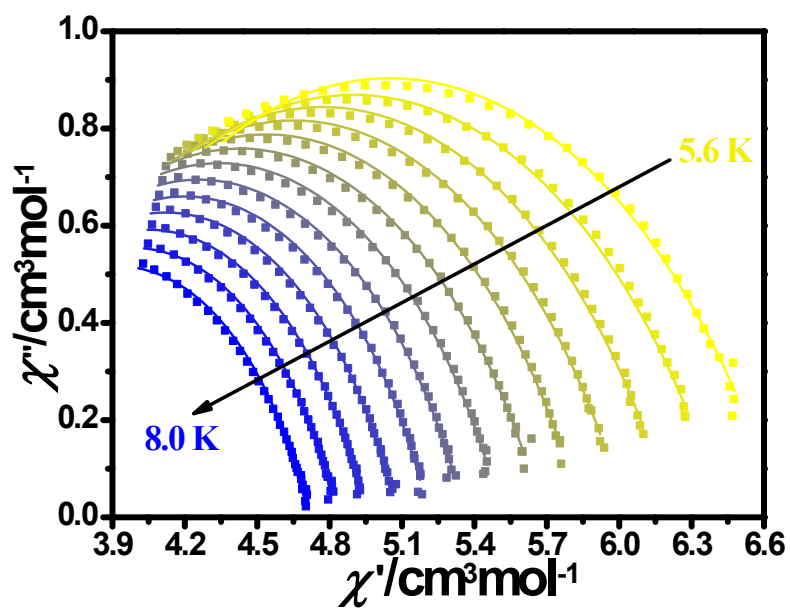
Figure S28. Cole-Cole plots of **1-Dy**.
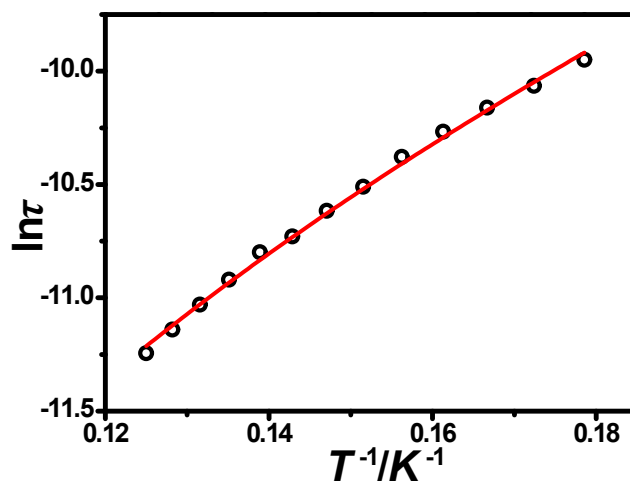
Figure S29. ln(τ)-T^{-1} of **1-Dy** with the best fit.
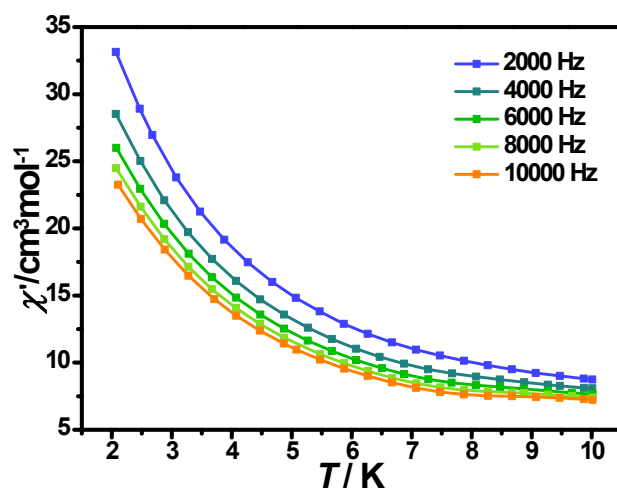
Figure S30. χ' (T) plot of **2-Dy** for frequence between 2000 and 10000 Hz in 0 Oe dc field.
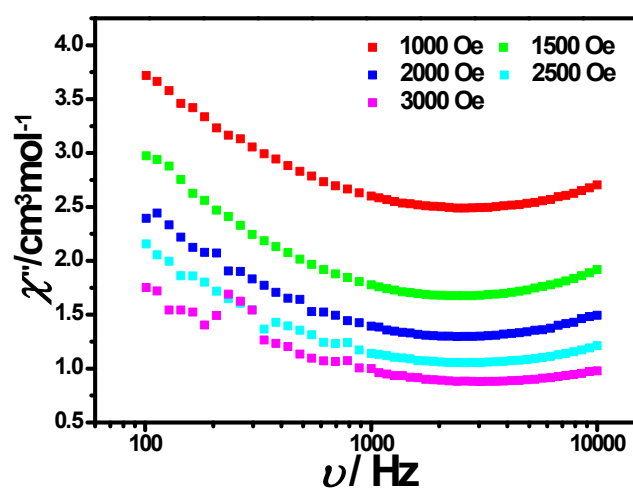
Figure S31. Frequency-dependent ac magnetic susceptibilities under externally applied dc fields at 2.2 K for **2-Dy**.

Table S6. Selected parameters from the fitting result of the Cole-Cole plots for **1-Dy** under 1000 Oe.

Temp. (K)	χ_S	χ_T	τ	α
5.6 K	3.191	0.00758	4.772E-5	0.356
5.8 K	3.082	0.00982	4.256E-5	0.343
6.0 K	3.004	0.0854	3.866E-5	0.332
6.2 K	2.935	0.1545	3.474E-5	0.323
6.4 K	2.861	0.2279	3.108E-5	0.313
6.6 K	2.805	0.2822	2.726E-5	0.310
6.8 K	2.730	0.3570	2.452E-5	0.299
7.0 K	2.667	0.4208	2.188E-5	0.294
7.2 K	2.574	0.5131	2.041E-5	0.274
7.4 K	2.517	0.5651	1.809E-5	0.273
7.6 K	2.459	0.6234	1.610E-5	0.271
7.8 K	2.399	0.6832	1.451E-5	0.270
8.0 K	2.339	0.7436	1.308E-5	0.269

$$\chi' = \chi_S + (\chi_T - \chi_S)\frac{1 + (\omega\tau)^{1-\alpha}sin(\frac{\alpha\pi}{2})}{1 + 2(\omega\tau)^{1-\alpha}sin\left(\frac{\alpha\pi}{2}\right) + (\omega\tau)^{2-2\alpha}}$$

$$\chi'' = (\chi_T - \chi_S)\frac{(\omega\tau)^{1-\alpha}cos(\frac{\alpha\pi}{2})}{1 + 2(\omega\tau)^{1-\alpha}sin\left(\frac{\alpha\pi}{2}\right) + (\omega\tau)^{2-2\alpha}}$$

Equ. S1

χ_S = the adiabatic susceptibility (at infinitely high frequency of ac field),

χ_T = the isothermal susceptibility (at infinitely low frequency of ac field),

τ = the relaxation time,

α = the distribution (Cole-Cole) parameter,

and ω is an angular frequency, that is $\omega = 2\pi\nu$, with ν being for the linear frequency in [Hz] units

Table S7. Photothermal property in this work compared with previous reported solid lanthanide/transition metal-based materials.

Samples	Light source	Light Intensity	Temperature ranges	Added temperature	Normalized temperature raise in 0.1 W cm^{-2}	ref
Dy-BPyNIT	1064 nm NIR laser	0.1 W cm^{-2}	24.2-44.2 °C	20.0 °C in 3 min	20.0 °C in 3 min	**This work**
Dy-NITPzCH$_2$IM	1064 nm NIR laser	0.1 W cm^{-2}	19.6-38.8 °C	19.6 °C in 3 min	19.6 °C in 5 min	
La-MV-MOF(film)	808 nm NIR laser	2 W cm^{-2}	23.1-145.0 °C	121.9 °C in 200 s	6.08 °C in 200 s	[S5]
La-MV-MOF(cryst)	808 nm NIR laser	2 W cm^{-2}	23.1-111.1 °C	88 °C in 10 s	4.4 °C in 10 s	[S5]
Dy-2D-MOF	1 sun light	0.1 W cm^{-2}	29.2-63.9 °C	34.7 °C in 4 min	34.7 °C in 4 min	[S6]
Dy-*m*-TTFTB	808 nm NIR laser	0.1 W cm^{-2}	21.3-31.0 °C	9.7 °C in 15 s	9.7 °C in 15 s	[S7]
I$_3$·Dy-*m*-TTFTB	808 nm NIR laser	0.1 W cm^{-2}	21.3-54.9 °C	33.6 °C in 15 s	33.6 °C in 15 s	[S7]
S&I/LDH	808 nm NIR laser	0.5 W cm^{-2}	---	8.8 °C in 3 min	1.76 °C in 3 min	[S8]
EuTTA-350	420-2500 nm	0.1 W cm^{-2}	22.2-69.2 °C	47 °C in 480 s	47 °C in 480 s	[S9]
HKUST-1	300-650 nm	0.5 W cm^{-2}	25.0-124.7 °C	99.3 °C in 30 min	19.86 °C in 30 min	[S10]
UiO-66	300-650 nm	0.5 W cm^{-2}	25.5-57.3 °C	31.8 °C in 30 min	6.36 °C in 30 min	[S10]
UiO-66-NH$_2$	300-650 nm	0.5 W cm^{-2}	25.0-148.6 °C	123.6 °C in 30 min	24.72 °C in 30 min	[S10]
ZIF-8	300-650 nm	0.5 W cm^{-2}	26.1-70.5 °C	44.4 °C in 30 min	8.88 °C in 30 min	[S10]
ZIF-67	300-650 nm	0.5 W cm^{-2}	26.4-127.7 °C	101.3 °C in 30 min	20.26 °C in 30 min	[S10]
Fe-MIL-NH$_2$	300-650 nm	0.5 W cm^{-2}	27.6-143.4 °C	115.8 °C in 30 min	23.16 °C in 30 min	[S10]
IR-MOF-3	300-650 nm	0.5 W cm^{-2}	26.4-118.6 °C	92.2 °C in 30 min	18.44 °C in 30 min	[S10]
CPO-27-Mg	300-650 nm	0.5 W cm^{-2}	24.1-135.8 °C	111.7 °C in 30 min	22.34 °C in 30 min	[S10]
THPTS-Pb	1064 nm NIR laser	0.8 W cm^{-2}	29-93 °C	64 °C in 180 s	8 °C in 180 s	[S11]
Ag-2D-CPs	800 nm NIR laser	0.5 W cm^{-2}	------	24.5 °C in 3 min	4.9 °C in 3 min	[S12]
HPCM-4	1 sun light	0.1 W cm^{-2}	24-41.2 °C	17.8 °C in 60 min	17.8 °C in 60 min	[S13]
Cu mesh	1 sun light	0.1 W cm^{-2}	25-30.3 °C	5.3 °C in 40 s	5.3 °C in 40 s	[S14]
Cu(OH)$_2$ NWs on Cu	1 sun light	0.1 W cm^{-2}	25-40.7 °C	15.7 °C in 40 s	15.7 °C in 40 s	[S14]
Cu-CAT-1 MOF	1 sun light	0.1 W cm^{-2}	25-53.2 °C	28.2 °C in 40 s	28.2 °C in 40 s	[S14]
Ag-TEPE-AC	808 nm NIR laser	1 W cm^{-2}	25.3-160 °C	134.7 in 30 s	13.4 in 30 s	[S15]

Assumption of the added temperature is in direct proportion to light intensity for approximate comparison. This column will give the value of the normalized temperature raise for these materials irradiated with the light of 0.1 W

cm^{-2}. The raised temperatures were recorded when samples reached the steady-state, in which the temperature hardly raises by further illumination.

Conversion efficiency calculation

The conversion efficiency was determined according to previous method [S16]. Details are as follows: Based on the total energy balance for this system:

$$\sum_i m_i C_{pi} \frac{dT}{dt} = Q_s - Q_{loss}$$

where m$_i$ (0.275 g for **1-Dy** and 0.275 g for **2-Dy**) and $C_{p,i}$ (0.8 J (g°C) $^{-1}$) are the mass and heat capacity of system components, respectively. Q_s is the photothermal heat energy input by irradiating NIR laser to samples, and Q_{loss} is thermal energy lost to the surroundings. When the temperature is maximum, the system is in balance.

$$Q_s = Q_{loss} = hS\Delta T_{max}$$

where h is heat transfer coefficient, S is the surface area of the container, ΔT_{max} is the maximum temperature change. The photothermal conversion efficiency η is calculated from the following equation:

$$\eta = \frac{hS\Delta T_{max}}{I(1 - 10^{-A_{1064}})}$$

where I is the laser power (power density, 0.1 W cm^{-2}) and A_{1064} is the absorbance of the sample (0.275 g) at the wavelength of 1064 nm (**1-Dy**: $A'_{1064} = 0.124$ for 0.02 g; **2-Dy**: $A'_{1064} = 0.115$ for 0.02 g). In order to obtain the hS, a dimensionless driving force temperature, θ is introduced as follows:

$$\theta = \frac{T - T_{surr}}{T_{max} - T_{surr}}$$

where T is the temperature of sample, T_{max} is the maximum system temperature, and T_{surr} is the initial temperature.

The sample system time constant τs:

$$\tau_s = \frac{\sum_i m_i C_{p,i}}{hS}$$

thus
$$\frac{d\theta}{dt} = \frac{1}{\tau_s} \frac{Q_s}{hS\Delta T_{max}} - \frac{\theta}{\tau_s}$$

when the laser is off, Qs = 0, therefore $\dfrac{d\theta}{dt} = -\dfrac{\theta}{\tau_s}$,and $t = -\tau_s \ln\theta$

so hS could be calculated from the slope of cooling time vs $\ln\theta$.

The detailed calculation results of each parameter are shown in the following table.

Table S8. The detailed calculation results of photothermal conversion efficiency η.

	m_i / g	T_{surr} / °C	T_{max} / °C	τ_s / S	hS	η
1-Dy	0.275	24.2	44.2	60.09	0.00366	74.09%
2-Dy	0.275	19.6	38.8	75.70	0.00290	56.99%

References

[S1] E. F. Ullman, L. Call, J. H. Osiecki, Stable free radicals. VIII. New imino, amidino, and carbamoyl nitroxides. *J. Org. Chem.* 1970, **35**, 3623-3631.

[S2] G. M. Sheldrick, SHELXS-2014, Program for Structure Solution; Universitat of Göttingen: Germany, 2014.

[S3] G. M. Sheldrick, SHELXL-2014, Program for Structure Reffnement; Universitat of Göttingen: Germany, 2014.

[S4] A. L. Spek, Single-crystal structure validation with the program PLATON. *J. Appl. Crystallogr.* 2003, **36**, 7-13.

[S5] S. Wang, S. Li, J. Xiong, Z. Lin, W. Wei, Y. Xu, Near-infrared photothermal conversion of stable radicals photoinduced from a viologen-based coordination polymer. *Chem. Commun.* 2020, **56**, 7399-7402.

[S6] J. Su, N. Xu, R. Murase, Z. M. Yang, D. M. DQAlessandro, J. L. Zuo, J. Zhu, Persistent Radical Tetrathiafulvalene-Based 2D Metal-Organic Frameworks and Their Application in Efficient Photothermal Conversion. *Angew. Chem. Int. Ed.* 2021, **60**, 4789-4795.

[S7] J. Su, P. Y. Cai, T. Yan, Z. M. Yang, S. Yuan, J. L. Zuo, H. C. Zhou, Enhancing the photothermal conversion of tetrathiafulvalene-based MOFs by redox doping and plasmon resonance. *Chem. Sci.* 2022, **13**, 1657-1664.

[S8] X. Mei, J. L. Ma, X. Bai, X. Zhang, S. M. Zhang, R. Z. Liang, M. Wei, D. G. Evans, X. Duan, A bottom-up synthesis of rare-earth-hydrotalcite monolayer nanosheets toward multimode imaging and synergetic therapy. *Chem. Sci.* 2018, **9**, 5630-5639.

[S9] X. H. Ye, L. H. Chung, K. Li, S. Zheng, Y. L. Wong, Z. H. Feng, Y. H. He, D. Chu, Z. T. Xu, L. Yu, J. He, Organic radicals stabilization above 300° C in Eu-based coordination polymers for solar steam generation. *Nat Commun.* 2022, **13**, 6116.

[S10] J. Espin, L. Garzon-Tovar, A. Carne-Sanchez, I. Imaz, D. Maspoch, Photothermal activation of metal–organic frameworks using a UV-vis light source. *ACS Appl. Mater. Interfaces.* 2018, **10**, 9555-9562.

[S11] J. Z. Liao, Z. C. Zhu, S. T. Liu, H. Ke, Photothermal Conversion Perylene-Based Metal-Organic Framework with Panchromatic Absorption Bandwidth across the Visible to Near-Infrared. *Inorg. Chem.* 2024, **63**, 3327-3334.

[S12] M. Q. Li, M. Zhao, L. Y. Bi, Y. Q. Hu, G. Gou, J. Li, Y. Z. Zheng, Two-dimensional silver (I)-dithiocarboxylate coordination polymer exhibiting strong near-infrared photothermal effect. *Inorg. Chem.* 2019, **58**, 6601-6608.

[S13] X. Ma, W. Fang, Y. Guo, Z. Li, D. Chen, W. Ying, Z. Xu, C. Gao, X. Peng, Hierarchical porous SWCNT stringed carbon polyhedrons and PSS threaded MOF bilayer membrane for efficient solar vapor generation. *Small.* 2019, **15**, 1900354.

[S14] Q. Ma, P. Yin, M. Zhao, Z. Luo, Y. Huang, Q. He, Y. Yu, Z. Liu, Z. Hu, B. Chen, H. Zhang, MOF-based hierarchical structures for solar-thermal clean water production. *Adv. Mater.* 2019, **31**, 1808249.

[S15] P. Y. Liao, J. X. Li, J. C. Liu, Q. Xiong, Z. Y. Ruan, T. Li, W. Deng, S. D. Jiang, J. H. Jia, M. L. Tong, Radical-Induced Photochromic Silver(I) Metal-Organic Frameworks: Alternative Topology, Dynamic Photoluminescence and Efficient Photothermal Conversion Modulated by Anionic Guests. *Angew. Chem. Int. Ed.* 2024, e202401448.

[S16] B. Lü, Y. Chen, P. Li, B. Wang, K. Müllen, M. Yin, Stable radical anions generated from a porous perylenediimide metal-organic framework for boosting near-infrared photothermal conversion. *Nat. Commun.* 2019, **10**, 767.